



Phase Transformation and Intense 2.7 μm Emission from Er^{3+} Doped YF_3/YOF Submicron-crystals

Guanqi Chai, Guoping Dong, Jianrong Qiu, Qinyuan Zhang & Zhongmin Yang

State Key Laboratory of Luminescent Materials and Devices, and Institute of Optical Communication Materials, South China University of Technology, Guangzhou 510641, PR China.

Yttrium fluoride $\text{YF}_3:\text{Er}^{3+}$ and yttrium oxyfluoride $\text{YOF}:\text{Er}^{3+}$ submicron-crystals with mid-infrared fluorescent emissions were synthesized for the first time. The rhombohedral phase YOF submicron-crystals were synthesized by the crystalline phase transformation from pure orthorhombic YF_3 submicron-crystals, which were prepared by co-precipitation method. The composition and morphology were characterized by X-ray diffraction (XRD), scanning electron microscope (SEM) and transmission electron microscopy (TEM), which showed that submicron-crystals were quasi-spherical with the particle size of ~ 400 nm. A novel formation mechanism of YOF submicron-crystals was proposed. Photoluminescence (PL) spectra indicated the 2.7 μm emission of Er^{3+} has remarkably enhanced with the increase of Er^{3+} doping concentration, and a novel dynamic circulatory energy transfer mechanism was proposed. Fourier transform infrared spectra (FTIR) were used to demonstrate the change of hydroxyl content. These oxyfluoride submicron-crystals provide a new material for nano/submicron-crystals-glass composites, and open a brand new field for the realization of mid-infrared micro/nano-lasers.

In recent years, solid state lasers operating around 2.7 μm have attracted more and more attention due to their potential applications in various fields, such as remote sensing, atmosphere pollution monitoring, and military, etc¹⁻⁵. However, during the research process of mid-infrared lasers, there are many kinds of problems which restrict their development, such as the luminous efficiency of rare-earth ions, the stability of host materials, etc⁶. Thus, it is extremely important to search for a new solid state material to solve these problems. Nano/submicron-crystals, as the candidate hosts for mid-infrared fluorescence and laser, have attracted great attention due to their superior characteristics compared with conventional glass and glass ceramics materials, such as higher luminous efficiency, smaller particle size, higher chemical stability and more mature synthesis methods, etc⁷⁻¹⁰. Thus, rare-earth ions doped nano/submicron-crystals, which can be combined with glass matrixes to form nano/submicron-crystals-glass composites for fiber-drawing¹¹⁻¹², open a brand new field for the realization of mid-infrared micro/nano-lasers.

Up to now, mid-infrared fluorescence can be achieved in many kinds of rare-earth ions and get intensive study¹³, such as Er^{3+} ¹⁴, Ho^{3+} ¹⁵, and Dy^{3+} ¹⁶, etc. Among all the rare-earth ions, Er^{3+} fluorescence emitting at 2.7 μm , due to the $^4I_{11/2} \rightarrow ^4I_{13/2}$ transition, plays a key role in the investigations and has been achieved in many kinds of glasses¹⁷⁻²⁰, glass ceramics²¹ and single-crystals²² hosts. However, many kinds of factors must be considered in order to obtain high mid-infrared luminous efficiency²³. Among them, a minimal absorption coefficient in the typical H_2O absorption band around 3 μm and lower phonon energy of the host materials are the extremely important influencing factors²⁴. This is because that the mid-infrared fluorescence can be absorbed by the hydroxyl groups (OH^-) and undetected. Moreover, the higher phonon energy of host materials could result in the increase of the nonradiative transition between the two energy levels ($^4I_{11/2}$ and $^4I_{13/2}$) of Er^{3+} ions, and subsequently decrease the radiative transition of 2.7 μm emission. Therefore, choosing a right material as mid-infrared luminous host materials is especially important in this research.

Oxide and fluoride nano/submicron-crystals as two major kinds of micro/nano-materials have been extensive studied in many fields²⁵⁻²⁶. The results confirm that, oxide nano/submicron-crystals have better mechanical strength and chemical stability, but higher phonon energy (larger than 500 cm^{-1})²⁷, and fluoride nano/submicron-crystals have lower phonon energy, but chemically and thermally unstable²⁸. However, oxyfluorides nano/submicron-crystals combine the advantages of both fluoride and oxide nano/submicron-crystals, such as they can show better chemical and thermal stability than fluorides, and lower phonon energy than oxides, so that it will be

SUBJECT AREAS:

NANOPHOTONICS AND
PLASMONICS

OPTICAL MATERIALS

SYNTHESIS AND PROCESSING

NANOPARTICLES

Received

28 December 2012

Accepted

15 March 2013

Published

22 April 2013

Correspondence and requests for materials should be addressed to G.P.D. (dgp@scut.edu.cn) or Z.M.Y. (yangzm@scut.edu.cn)



desired as ideal mid-infrared host materials^{29–31}. Yttrium fluoride (YF₃) is one of most promising materials as a kind of the down/up conversion materials, due to their wider optical transmission window and the minimization of the excited state quenching of rare-earth ions³², especially it has lower phonon energy ($\sim 350\text{ cm}^{-1}$)³³. Yttrium oxyfluoride (YOF) as a typical oxyfluoride with a phonon energy of $\sim 400\text{ cm}^{-1}$, not only contains the advantages of YF₃, but also has other unique advantages, such as excellent chemical and thermal stability than YF₃. Thus, YOF nano/submicron-crystals are chosen as an ideal matrix material for mid-infrared fluorescence in this study. Furthermore, due to so much OH⁻ exist in the structure of nano/submicron-crystals, which is unavoidable in the chemical synthesis process, there have been no any reports about the mid-infrared fluorescence emissions from fluoride or oxyfluorides nano/submicron-crystals so far. Thus, search a novel routine to solve the OH⁻ absorption problem (dehydration) is extremely important for the mid-infrared fluorescence emissions of crystal particles in this study.

At present, there are many wet chemical methods to synthesize YF₃ and YOF nano/submicron-crystals, including microemulsion³⁴, co-precipitation^{35,36}, sol-gels³⁷ and hydrothermal³⁸ method. And all these chemical processes achieve homogeneous mixing of activator cations on the atomic level, leading to an increase in reaction rate and lowering synthesis temperature. Among these synthesis methods, co-precipitation method has more superiority, because it is a more milder and mature chemical reaction, as well as higher repeatability and larger production. Moreover, it uses ammonium hydrogen fluoride (NH₄HF₂) as the precipitator, so that during the process of temperature rise, the OH⁻ in the structure of crystal particles can be removed effectively by the hygroscopic property of NH₄HF₂. Thus, co-precipitation method is chosen as the synthesis method in this study, which is also beneficial to the preparation of nano/submicron-crystals-glass composites¹¹ in the future.

Herein, the preparation of YOF:Er³⁺ submicron-crystals with mid-infrared fluorescence is reported for the first time. The YOF:Er³⁺ submicron-crystals were synthesized on the basis of the YF₃:Er³⁺ submicron-crystals with good morphology by co-precipitation

method and continuous calcining method. During the calcining process, utilized the hygroscopic property of fluoride and instability of YF₃:Er³⁺ submicron-crystals, YF₃:Er³⁺ submicron-crystals were transformed into YOF:Er³⁺ submicron-crystals free of OH⁻. The possible formation mechanism has been discussed in detail. Based on the luminescence characteristics of submicron-crystals with different Er³⁺ doping concentrations, as well as the change of Er³⁺:⁴I_{11/2} and ⁴I_{13/2} levels lifetime, a novel dynamic circulatory energy transfer mechanism of Er³⁺ in YOF submicron-crystals has been tentatively proposed.

Results

Structural and phase investigations of YF₃:Er³⁺ and YOF:Er³⁺ submicron-crystals. Fig. 1 shows XRD patterns of 4 mol% Er³⁺ doped fluoride precursor powders calcined at different temperatures and several diffraction peaks are observed. From the patterns, when the temperature is 400 °C and 600 °C, almost all the diffraction peaks are in agreement with the standard card of the orthorhombic phase YF₃ (JCPDF: 74-0911). With the increase of temperature, an obvious phase transformation has occurred, and when the temperature reaches 1100 °C, the products present the pure rhombohedral phase YOF (JCPDF: 71-2100). It illustrates that YF₃ submicron-crystals have successfully transformed into YOF submicron-crystals with the increase of temperature. But further increase of temperature will result in the occurrence of a little impure phase, Y₂O₃ (JCPDF: 20-1412). This is because that with the increase of temperature, fluoride become so instability that F ions in YF₃ crystal lattice can be oxidized gradually due to the oxygen in the environment, which is beneficial for oxygen atoms replacing fluorine atoms and entering into crystals lattice. And the content of oxygen atoms in crystals lattice has a remarkable increase with the increase of temperature, which results in the formation of Y₂O₃, as shown in Fig. 1. Thus, the increase of temperature from 600 °C to 1200 °C resulted in a substantial decrease in the YF₃ phase and the appearance of a new phase, YOF, to the detriment of Y₂O₃. Moreover, with the increase of temperature, the diffraction peaks grow stronger and the full width at half maximum (FWHM) of the peaks become narrower, indicating the growth of crystalline particles with better crystallinity. Therefore, we choose precursor powders

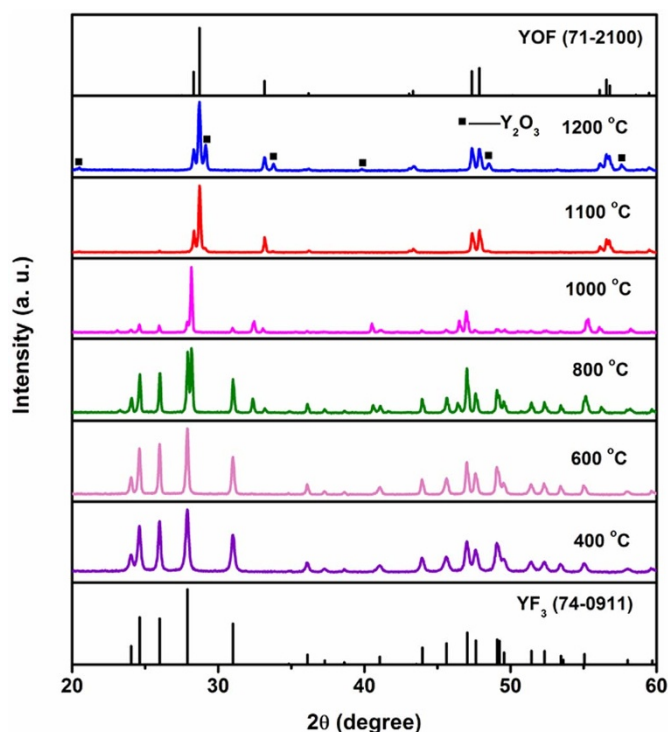


Figure 1 | XRD patterns of 4 mol% Er³⁺ doped fluoride precursor powders calcined at different temperatures for 2 h.

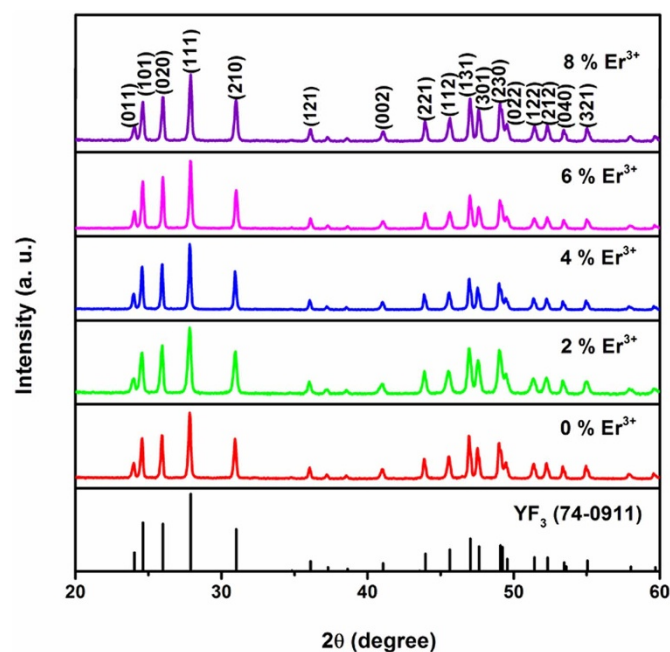


Figure 2 | XRD patterns of YF₃ submicron-crystals (calcined at 600 °C for 2 h) doped with different Er³⁺ concentrations.

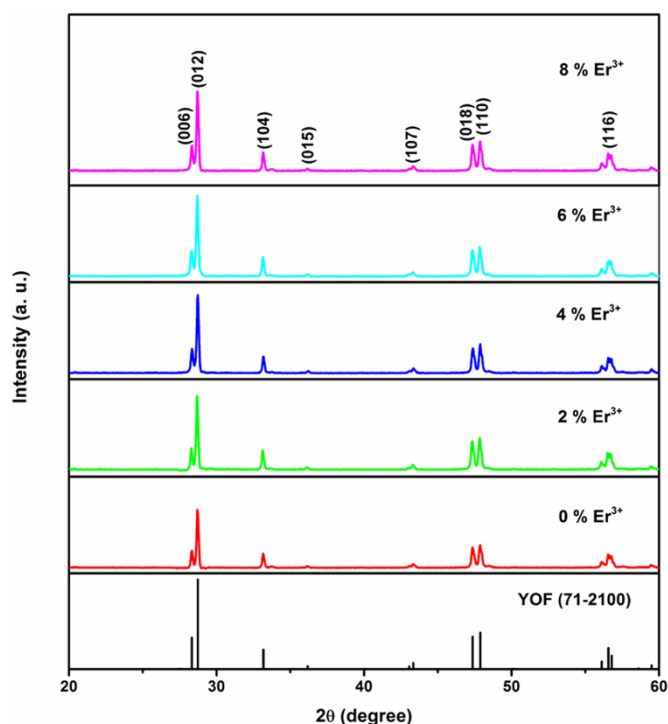


Figure 3 | XRD patterns of YOF submicron-crystals (calcined at 1100°C for 2 h) doped with different Er^{3+} concentrations.

calcined at 600°C and 1100°C for 2 h to form pure $\text{YF}_3:\text{Er}^{3+}$ and $\text{YOF}:\text{Er}^{3+}$ submicron-crystals as the typical synthesis condition in the following text.

Fig. 2 and Fig. 3 show XRD patterns of different concentration of Er^{3+} doped YF_3 and YOF submicron-crystals, respectively. In Fig. 2, when the temperature is 600°C, all the diffraction peaks can be assigned to the orthorhombic phase YF_3 (JCPDF: 74-0911) and the addition of Er^{3+} almost has no effect on the phase of submicron-crystals products. Similarly, when the temperature is 1100°C, all the

diffraction peaks can be assigned to the rhombohedral phase YOF (JCPDF: 71-2100) and no other impurity phase is detected, as shown in Fig. 3. Besides, with the increase of Er^{3+} doping concentration, the diffraction peaks have a little shifting to higher 2θ region, which indicates that Er^{3+} with smaller ionic radius have replaced Y^{3+} and entered into YF_3 and YOF crystals lattice, respectively. It is worth mentioning that, in this study, the doping concentration of rare-earth ions in all samples is only titular concentration.

Morphology of $\text{YF}_3:\text{Er}^{3+}$ and $\text{YOF}:\text{Er}^{3+}$ submicron-crystals. The SEM images of 4 mol% Er^{3+} doped fluoride precursor powders calcined at different temperatures are shown in Fig. 4a–f. During the process of temperature rise, the morphology has an obvious change, along with crystalline phase transformed from pure orthorhombic YF_3 phase into pure rhombohedral YOF phase^{39,40}. A schematic illustration of the transformation process is shown in Fig. 4g and the possible formation mechanism is proposed as follows. When the temperature is rose from 400°C to 600°C, the average size of YF_3 submicron-crystals with better dispersity is grown to about 300–400 nm and presents quasi-spherical morphology (Fig. 4b), as the process of “(1) Growing”. When the temperature reaches 800°C, due to oxygen atoms join in the crystal formation and growth, the crystalline phase is forced to be transformed from fluoride into oxyfluoride. But this temperature is still lower and cannot provide enough energy for the formation of pure YOF crystal nucleus, so that only an agglomerate and self-assemble process happens under the effect of oxygen atoms, and the average size reaches up to 1–2 μm (Fig. 4c), as the process of “(2) Self-assemble”. However, when the temperature is 1000°C or 1100°C, there are enough energy and oxygen atoms for the formation and growth of YOF crystal nucleus, and this formation process can be rationally explained by a dissolution-recrystallization mechanism^{41,42}. Herein, under this higher temperature, sufficient oxygen atoms enter into crystal lattices and result in the formation and growth of YOF crystal nucleus (Fig. 4d). Finally, pure rhombohedral YOF phase have formed at 1100°C, and the average size of YOF submicron-crystals is about 400 nm (Fig. 4e), as the process of “(3) Dissolution-Recrystallization”. Then, with the future increase of temperature to

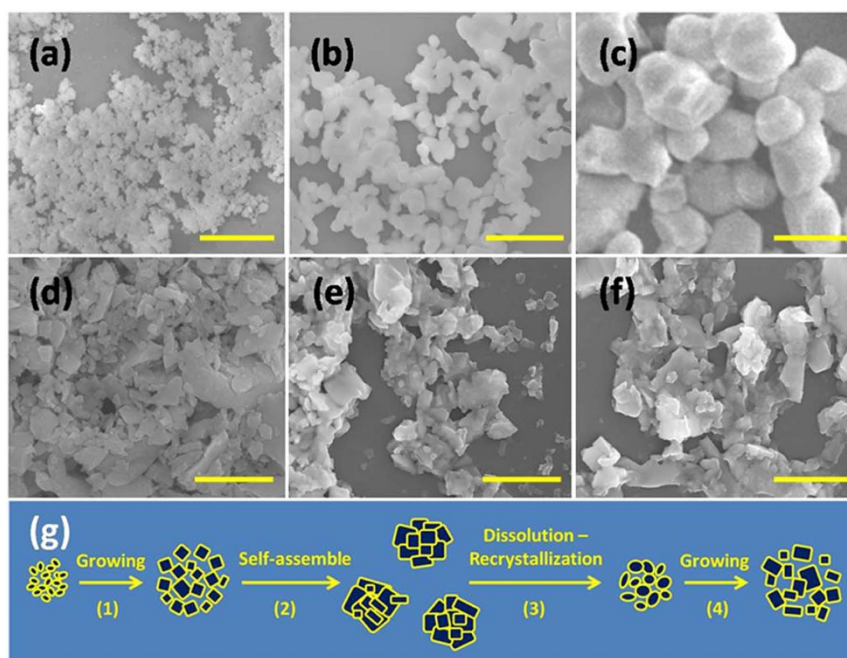


Figure 4 | SEM images of 4 mol% Er^{3+} doped fluoride precursor powders calcined at different temperatures for 2 h. (a) 400°C, (b) 600°C, (c) 800°C, (d) 1000°C, (e) 1100°C and (f) 1200°C. All of the scale bars are 2 μm . (g) Schematic illustration for the formation process of YOF submicron-crystals.

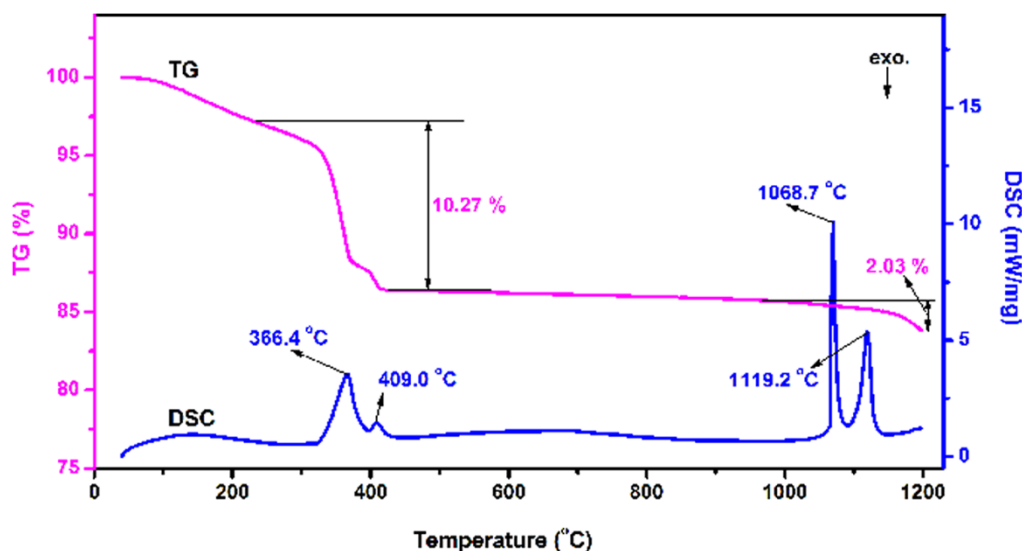


Figure 5 | TG-DSC curves of the fluoride precursor powders in air atmosphere with a heating rate of $10^{\circ}\text{C}/\text{min}$.

1200°C , interfacial boundary diffusion is occurred and grain size grow slightly (Fig. 4f), as the process of “(4) Growing”.

In order to further prove the “phase transformation” between the YF_3 and YOF crystalline phase, the thermogravimetry-differential scanning calorimetry (TG-DSC) curves of the fluoride precursor powders in air atmosphere with a heating rate of $10^{\circ}\text{C}/\text{min}$ are shown in Fig. 5. The DSC curve exhibits two endothermic peaks around 366.4°C and 409.0°C which is due to the formation of the YF_3 crystalline phase, and this result agrees well with the XRD result that YF_3 crystalline begin to form at $\sim 400^{\circ}\text{C}$ (as the XRD pattern shown in Fig. 1). At the same time, during this process, the weight has lost about 10.27% due to the dehydration and vaporization of many kinds of fluoride by-products and residual organics. Moreover, there is also an intense endothermic peak at 1068.7°C due to the formation of YOF crystalline phase which is in accordance with the XRD result that YOF crystalline begin to form at $\sim 1000^{\circ}\text{C}$ and complete the phase transformation process at $\sim 1100^{\circ}\text{C}$ (as the XRD patterns shown in Fig. 1). The endothermic peak at 1119.2°C is due to the formation of a little of Y_2O_3 crystalline phase which also agrees well with the XRD result that a little Y_2O_3 crystalline begin to form at $\sim 1200^{\circ}\text{C}$ (as the XRD pattern shown in Fig. 1). And during this process, the weight of the sample has lost about 2.03% due to the more and more oxygen atoms have replaced fluoride atoms and joined in YOF crystal lattice, which can promote the phase transformation process. Form the above results, it is surprising that the TG- DSC results agree well with the XRD results, which confirm the formation and phase transformation of YF_3 , YOF and Y_2O_3 crystalline. It is worth mentioning that, due to the rapid heating rate ($10^{\circ}\text{C}/\text{min}$) and short holding time during TG-DSC measurement, a slight error is found between the formation and phase transformation temperature in TG-DSC curves and XRD patterns.

Fig. 6a–d shows SEM images of different concentrations of Er^{3+} doped YF_3 submicron-crystals synthesized by co-precipitation method at 600°C for 2 h. With the increase of Er^{3+} doping concentration, the morphology almost have no obvious change and the average size of YF_3 submicron-crystals is maintained as $300\sim 400$ nm. Therefore, it can be deduced that the increase of Er^{3+} doping concentration have no obvious effect on the average size and morphology of YF_3 submicron-crystals. And the similar results are also confirmed in different Er^{3+} concentrations doped YOF submicron-crystals synthesized at 1100°C for 2 h (not illustrated).

Fig. 7a shows the HR-TEM image of $\text{YF}_3:\text{Er}^{3+}$ submicron-crystals. The crystal lattice fringes with some different spacing d values of

~ 0.166 nm and ~ 0.288 nm can be measured directly, which corresponds to the (321) and (210) crystal facets of the orthorhombic phase YF_3 , respectively. The selected area electron diffraction (SAED) pattern corresponding to the individual $\text{YF}_3:\text{Er}^{3+}$ submicron-crystals is shown in Fig. 7b, which indicates the individual $\text{YF}_3:\text{Er}^{3+}$ submicron-crystals exhibit a single crystalline character. The EDS spectrum of $\text{YF}_3:\text{Er}^{3+}$ submicron-crystals is also illustrated in Fig. 7c. In the picture, the peaks assigned to designed elements (i.e. Y, F and Er) are clearly observed. Besides the Si peak from the silicon wafer used to pick up the sample in the course of EDS measurement, no other impurity is detected. Thus, the result indicates that the $\text{YF}_3:\text{Er}^{3+}$ submicron-crystals are mainly consisted of Y, F and Er elements.

Fig. 8a shows the HR-TEM image of YOF: Er^{3+} submicron-crystals, which includes a series of crystals facets. Four kinds of crystal lattice fringes with the spacing d values of ~ 0.248 nm, ~ 0.310 nm, ~ 0.323 nm and ~ 0.269 nm are observed, which corresponds to the (015), (012), (101) and (104) crystal facets of the

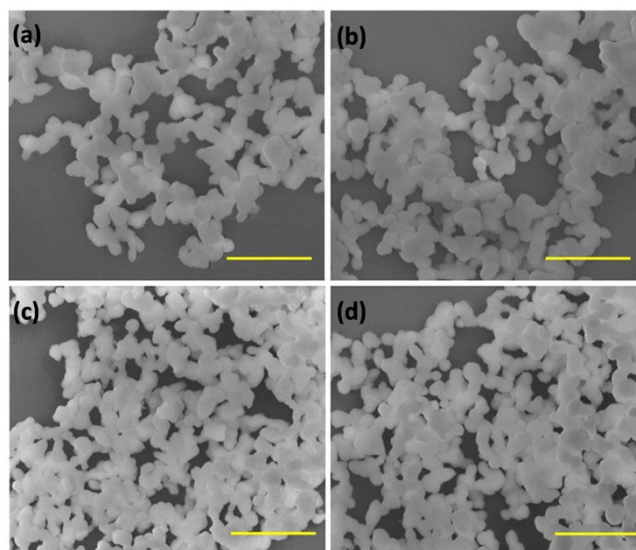


Figure 6 | SEM images of YF_3 submicron-crystals (calcined at 600°C for 2 h) doped with different Er^{3+} concentrations. (a) 0 mol%, (b) 4 mol%, (c) 6 mol% and (d) 8 mol%. All of the scale bars are $2\ \mu\text{m}$.

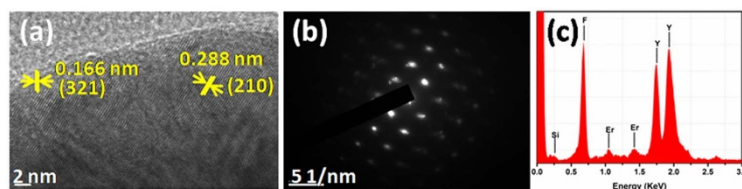


Figure 7 | (a) HR-TEM image and (b) SAED pattern of the $\text{YF}_3:\text{Er}^{3+}$ submicron-crystals, and the scale bar is 2 nm and 5 1/nm, respectively. (c) EDS spectrum of the $\text{YF}_3:\text{Er}^{3+}$ submicron-crystals. The presence of the Si peak results from the silicon wafer used to pick up the sample in the course of EDS measurement.

rhombohedral phase YOF (JCPDF: 71-2100), respectively. The SAED pattern corresponding to the $\text{YOF}:\text{Er}^{3+}$ submicron-crystals is shown in Fig. 8b. From the pattern, the $\text{YOF}:\text{Er}^{3+}$ submicron-crystals show a polycrystalline character. The diffraction rings can be indexed to the (006), (104), (107) and (10 10) crystal facets of the rhombohedral phase YOF, respectively. The EDS spectrum of $\text{YOF}:\text{Er}^{3+}$ submicron-crystals is also illustrated in Fig. 8c. In the picture, the peaks assigned to designed elements (i.e. Y, O, F and Er) are clearly observed. Besides the Si peak from the silicon wafer used to pick up the sample in the course of EDS measurement, no other impurity is detected. Thus, these result indicates that the $\text{YOF}:\text{Er}^{3+}$ submicron-crystals are mainly consisted of Y, F, O and Er elements.

Dehydration investigation of $\text{YF}_3:\text{Er}^{3+}$ and $\text{YOF}:\text{Er}^{3+}$ submicron-crystals. During the process of chemical synthesis, NH_4HF_2 with better hygroscopic property are used to remove the OH^- in the structure of crystal particles, which is benefit for the detection of mid-infrared emissions. The process and mechanism of dehydration can be described as follows. At higher temperature (about 100°C), multiple fluorides were formed and existed in the mixture precursor powders, such as hydrogen fluoride (HF) and ammonium fluoride (NH_4F), due to the chemical dynamic balance by the following equations, $\text{NH}_4\text{HF}_2 \rightarrow \text{HF} + \text{NH}_4\text{F}$ and $2\text{NH}_4\text{F} \rightarrow \text{NH}_4\text{HF}_2 + \text{NH}_3$. When the temperature is above 175°C , a salt mixture, which is the excessive NH_4HF_2 and NH_4F retained in progressively lesser quantities of constituent water, could eventually be obtained. And the salt mixture is held very tenaciously and can only be removed until the temperature is higher than 200°C ⁴³. As a result, not only the OH^- in the crystal particles, but also the other fluoride by-products can be removed with the evaporation of the salt mixture¹¹.

In order to clarify the influence of NH_4HF_2 on the content of OH^- in the structure, the FTIR spectra of fluoride precursor powders calcined at different temperatures are recorded in Fig. 9. The band at approximately 1260 cm^{-1} can be assigned to the bending vibration of OH^- group, and it has remarkably decreased with the increase of temperature. And the same results are also obtained for the change of the stretching vibration of carbonate (CO_3^{2-}) group at approximately 1440 cm^{-1} . The bands in the range from 1000 cm^{-1} to 400 cm^{-1} are assigned to the vibrations of crystals molecular bonds, and they have an obvious change with the transformation of crystalline phase at different temperature. From the curves in the range of

1000 cm^{-1} to 400 cm^{-1} , the vibration cutoff wavenumber of YF_3 submicron-crystals (prepared at 600°C) is about 500 cm^{-1} and that of YOF submicron-crystals (prepared at 1100°C) is about 600 cm^{-1} , which is relevant with the phonon energy of nanocrystals⁴⁴. Thus, although the phonon energy of YOF submicron-crystals is a little higher than that of YF_3 submicron-crystals, both YF_3 and YOF submicron-crystals have lower phonon energy.

Therefore, during the process of temperature rise, the OH^- in the structure of crystal particles is removed effectively through the hygroscopic property of NH_4HF_2 , which are very benefit for the detecting of mid-infrared fluorescence.

The mid-infrared emission of $\text{YF}_3:\text{Er}^{3+}$ and $\text{YOF}:\text{Er}^{3+}$ submicron-crystals. The mid-infrared emissions spectra of $\text{YOF}:\text{Er}^{3+}$ submicron-crystals prepared at 1100°C for 2 h are shown in Fig. 10. Due to the Stark levels split of rare-earth ions in crystalline hosts, the broadband emissions are split into many components. Under the pumping by a 976 nm LD, an emission at $2.7\text{ }\mu\text{m}$ due to the $\text{Er}^{3+}: ^4I_{11/2} \rightarrow ^4I_{13/2}$ transition is clearly observed as shown in Fig. 10. It is found that with the increase of Er^{3+} doping concentration from 0 to 4 mol% in YOF submicron-crystals, the emission intensity increases remarkably. However, with further increase of Er^{3+} doping concentration, the emission intensity gradually decreases. Thus, it can be deduced that the optimized single-doping concentration of Er^{3+} for $2.7\text{ }\mu\text{m}$ emission is 4 mol% in YOF submicron-crystals. Moreover, the $2.7\text{ }\mu\text{m}$ emission spectra of 4 mol% Er^{3+} doped fluoride precursor powders calcined at different temperatures are shown in Fig. 11. And the inset is enlarged image of mid-infrared fluorescence spectra of $\text{YF}_3:\text{Er}^{3+}$ submicron-crystals calcined at 400°C and 600°C for 2 h in the range from 2400 nm to 2900 nm, respectively. An obvious $2.7\text{ }\mu\text{m}$ mid-infrared emission is detected in $\text{YF}_3:\text{Er}^{3+}$ submicron-crystals for the first time. With the increase of temperature, the peak intensity for $2.7\text{ }\mu\text{m}$ emission remarkably increases. An intense $2.7\text{ }\mu\text{m}$ emission is obtained for YOF submicron-crystals prepared at 1100°C for 2 h. The noticeable enhancement of $2.7\text{ }\mu\text{m}$ emission with the increase of temperature can be ascribed into three main reasons as follows⁴⁵. Firstly, the submicron-crystals have more excellent crystallinity at higher temperatures. Secondly, the phase transition from YF_3 to YOF crystalline at higher temperatures more easily results in the fluorescence enhancement. Thirdly, the OH^- in the structure of crystal particles have been removed more thoroughly with the increase of calcination temperature, which is the

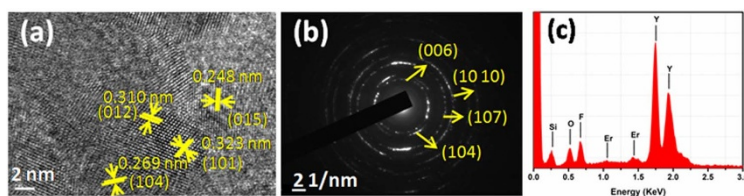


Figure 8 | (a) HR-TEM image and (b) SAED pattern of the $\text{YOF}:\text{Er}^{3+}$ submicron-crystals, and the scale bar is 2 nm and 2 1/nm, respectively. (c) EDS spectrum of the $\text{YOF}:\text{Er}^{3+}$ submicron-crystals. The presence of the Si peak results from the silicon wafer used to pick up the sample in the course of EDS measurement.

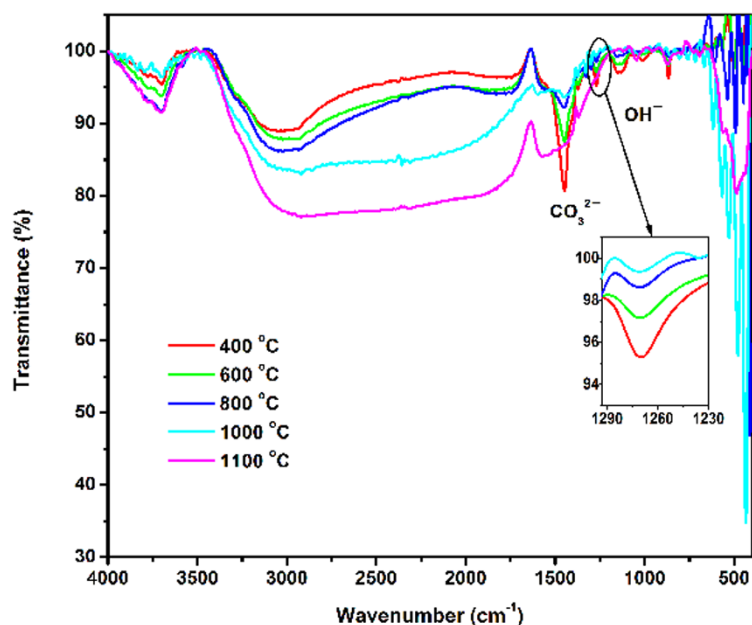


Figure 9 | The FTIR spectra of 4 mol% Er^{3+} doped fluoride precursor powders calcined at different temperatures for 2 h.

most major reason. Therefore, these three major factors result in that the luminous efficiency of YOF submicron-crystals prepared at 1100°C for 2 h is far better than that of YF_3 submicron-crystals prepared at 600°C for 2 h.

To investigate the luminescence mechanism of $2.7\ \mu\text{m}$ emission, we also investigated the $1.5\ \mu\text{m}$ near-infrared and up-conversion visible emissions of different Er^{3+} doping concentrations in YOF submicron-crystals. With the increase of Er^{3+} doping concentration in YOF submicron-crystals, an emission at $1.5\ \mu\text{m}$ due to the Er^{3+} : $^4I_{13/2} \rightarrow ^4I_{15/2}$ transition significantly decreases, as shown in Fig. 12. The up-conversion emissions of YOF: Er^{3+} submicron-crystals are shown in Fig. 13a. The green emissions at $520\ \text{nm}$ and $540\ \text{nm}$ are attributed to the Er^{3+} : $^4H_{11/2} \rightarrow ^4I_{15/2}$ and Er^{3+} : $^4S_{3/2} \rightarrow ^4I_{15/2}$ transitions, the red emissions at $640\ \text{nm}$ and $800\ \text{nm}$ are attributed to the Er^{3+} : $^4F_{9/2} \rightarrow ^4I_{15/2}$ and Er^{3+} : $^4I_{9/2} \rightarrow ^4I_{15/2}$ transitions. Ratios of the

intensity of green emission ($540\ \text{nm}$) to red emission ($640\ \text{nm}$), G/R are illustrated in Fig. 13b. From this figure, we can find that the value of G/R decreases monotonously with the Er^{3+} doping concentration changing from 2 to 8 mol%. And with the increase of Er^{3+} doping concentration, the intensity of the $800\ \text{nm}$ emission has a remarkable increase (Fig. 13c). Thus, these results indicate that the increase of Er^{3+} doping concentration in YOF submicron-crystals results in the decrease of the up-conversion and $1.5\ \mu\text{m}$ emissions, but increases the $2.7\ \mu\text{m}$ and $800\ \text{nm}$ emissions.

The $2.7\ \mu\text{m}$ emission of Er^{3+} is due to the $^4I_{11/2} \rightarrow ^4I_{13/2}$ transition, so the fluorescence decay curves of the $^4I_{13/2}$ ($1.5\ \mu\text{m}$ emission) and $^4I_{11/2}$ ($2.7\ \mu\text{m}$ emission) levels, as well as the fluorescence lifetime of the two levels, have been measured in Fig. 14 and Fig. 15. With the increase of Er^{3+} doping concentration, both the fluorescence lifetime

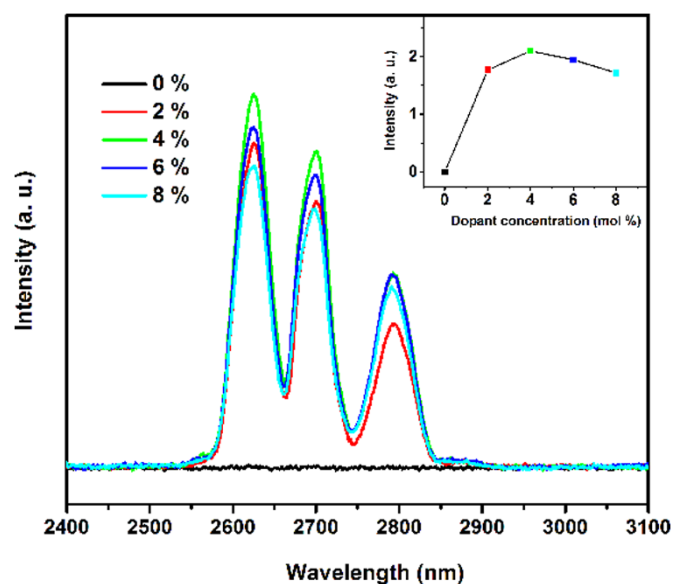


Figure 10 | The $2.7\ \mu\text{m}$ emission of $x\text{Er}^{3+}$ ($x = 0, 2, 4, 6, 8\ \text{mol}\%$) doped YOF submicron-crystals (calcined at 1100°C for 2 h). Inset: Er^{3+} concentration dependence of the peak intensity of the $2.7\ \mu\text{m}$ emission.

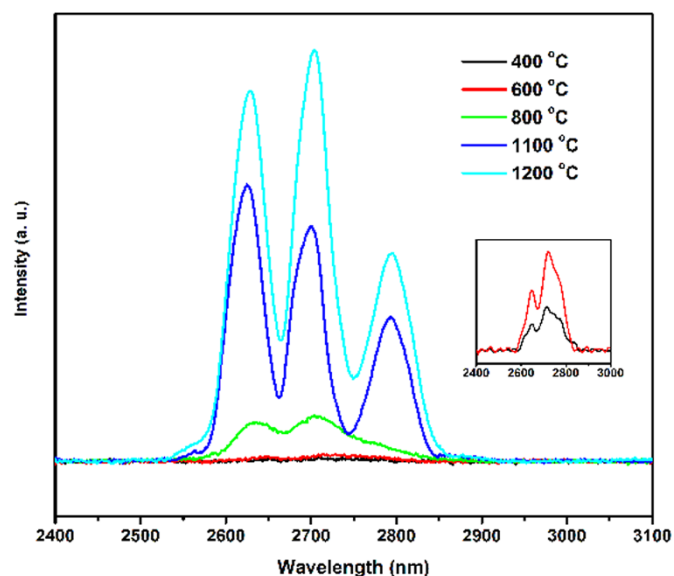


Figure 11 | The $2.7\ \mu\text{m}$ emission of 4 mol% Er^{3+} doped fluoride precursor powders calcined at different temperatures for 2 h. Inset: the enlarged image of the curves of $\text{YF}_3:\text{Er}^{3+}$ submicron-crystals (calcined at 400°C and 600°C for 2 h) in range from $2400\ \text{nm}$ to $3000\ \text{nm}$, respectively.

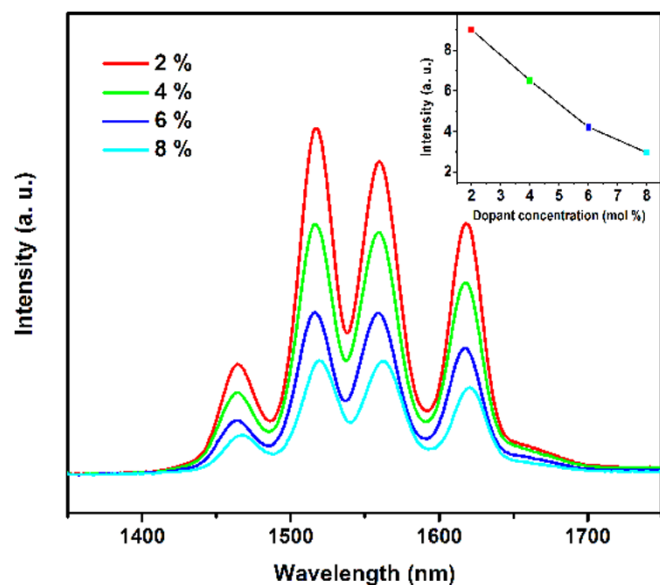


Figure 12 | The 1.5 μm emission of $x\text{Er}^{3+}$ ($x = 2, 4, 6, 8$ mol%) doped YOF submicron-crystals (calcined at 1100°C for 2 h). Inset: Er^{3+} concentration dependence of the peak intensity of the 1.5 μm emission.

of the $^4I_{11/2}$ and $^4I_{13/2}$ levels have remarkable decrease. The fluorescence lifetime of the lower level ($^4I_{13/2}$) is decreased from 10.28 ms to 4.14 ms, while that of the upper level ($^4I_{11/2}$) is decreased from 3.0 ms to 1.67 ms. Therefore, on these basis, it can be deduced that there should be several energy transfer processes between adjacent Er^{3+} ions, during the process of Er^{3+} doping concentration increasing.

Discussion

Obviously, with the increase of Er^{3+} doping concentration, the distance between Er^{3+} ions in YOF crystalline lattices is remarkably

decreased and this is benefit for electrons transition and energy recycling between adjacent Er^{3+} ions. Fig. 16 shows the energy levels diagram and possible energy transfer processes between two adjacent Er^{3+} ions. And a novel dynamic circulatory energy transfer mechanism is founded systematically as follows. Electrons in the $\text{Er}^{3+}:^4I_{15/2}$ level are excited to the $^4I_{11/2}$ level by the ground state absorption (GSA) process when sample is pumped by 976 nm LD. On one hand, some electrons in the $^4I_{11/2}$ level can undergo the excited state absorption (ESA1) and cross relaxation (CR3) processes to make the $^4F_{7/2}$ level populated. The excited electrons populated nonradiatively relax to the $^4H_{11/2}$, $^4S_{3/2}$ and $^4F_{9/2}$ levels, and generate the green and red emissions by radiatively relaxation. On the other hand, some electrons in the $^4I_{11/2}$ level can nonradiatively or radiatively relax to the $^4I_{13/2}$ level, and the radiation relaxation generates the 2.7 μm emission. Subsequently, the majority of electrons in the $^4I_{13/2}$ level can radiatively relax to generate the 1.5 μm emission. Moreover, some electrons in the $^4I_{13/2}$ level can undergo the ESA2 process to make a contribution to the green and red emissions, or transfer to the $^4I_{9/2}$ level by the CR1 process, which generate the 800 nm and 2.7 μm emissions. Moreover, the CR2 process can also change the status of the $^4I_{9/2}$ and $^4I_{13/2}$ levels. Based on the results discussed above, with the increase of Er^{3+} doping concentration, the possible energy transfer (ET) processes between the same energy levels of two adjacent Er^{3+} ions are more obvious and other energy transfer processes are more active. The ET1, ET2 and CR1 processes can compose a dynamic circulatory energy transfer process. During this process, the CR1 process is crucial importance⁴⁶, which well achieves the population inversion between the $^4I_{11/2}$ and $^4I_{13/2}$ levels, and makes the energy transfer between adjacent Er^{3+} ions more active, as well as increases the 2.7 μm emission between the two levels (Fig. 10). Meanwhile, due to the CR1 process, the intensity of the 800 nm emission increases (Fig. 13c), while that of the 1.5 μm emission decreases (Fig. 12). Moreover, due to the ET1, ET2 and CR1 processes, the transfer of electrons in the $^4I_{13/2}$ and $^4I_{11/2}$ levels between two adjacent Er^{3+} ions become an unusual active dynamic processes, so that the fluorescent lifetime of the two levels have a remarkable decrease (Fig. 14 and Fig. 15). And with the increase of Er^{3+} doping

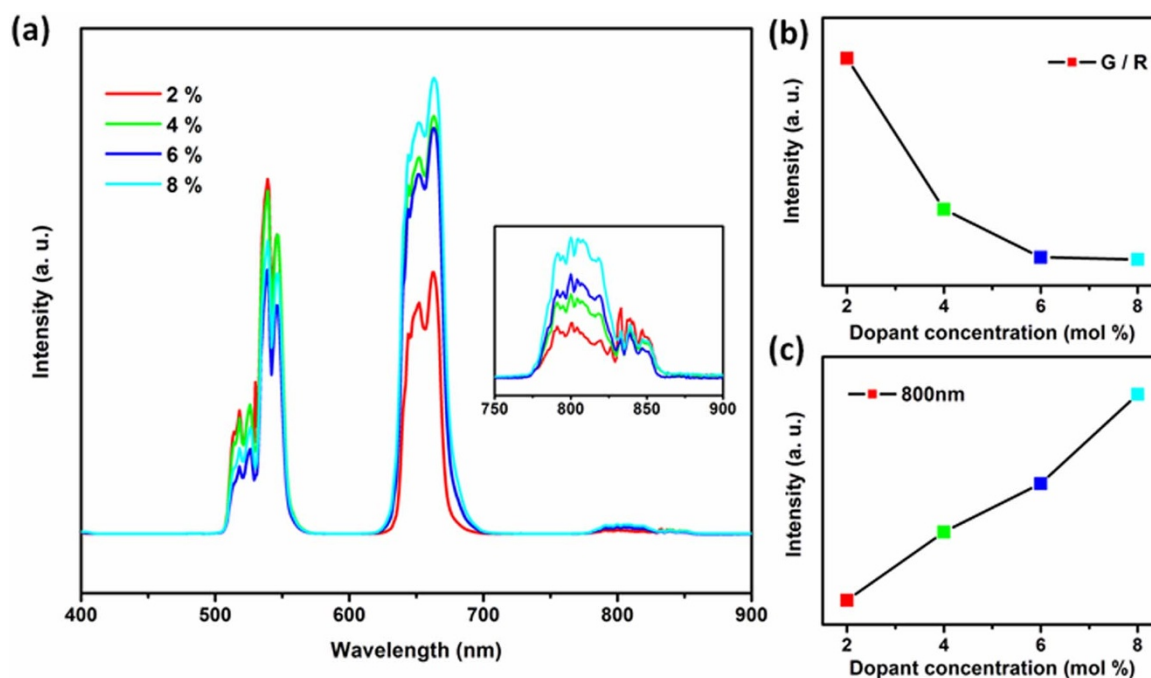


Figure 13 | (a) The up-conversion emissions of $x\text{Er}^{3+}$ ($x = 2, 4, 6, 8$ mol%) doped YOF submicron-crystals (calcined at 1100°C for 2 h). Inset: the enlarged image of the curves in range from 750 nm to 900 nm. (b) Ratio of the intensity of green emission (540 nm) to red emission (640 nm), G/R versus Er^{3+} concentration. (c) The peak intensity of the 800 nm emission versus Er^{3+} concentration.

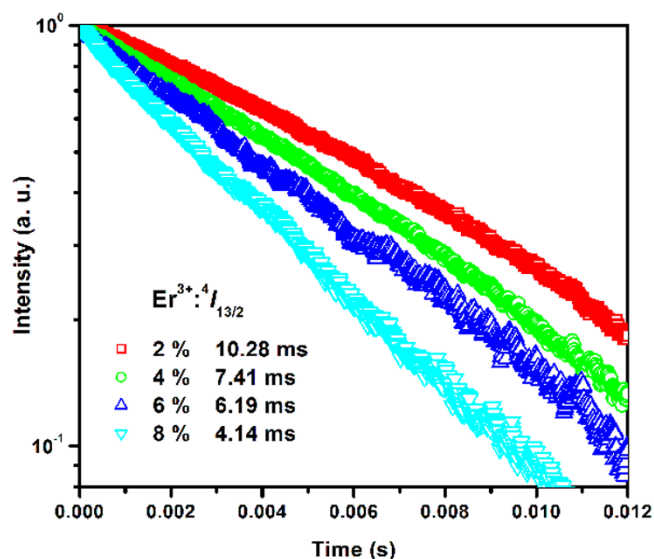


Figure 14 | The fluorescence decay curves of the $\text{Er}^{3+}:^4I_{13/2}$ level ($1.5 \mu\text{m}$ emission) in $x\text{Er}^{3+}$ ($x = 2, 4, 6, 8 \text{ mol}\%$) doped YOF submicron-crystals (calcined at 1100°C for 2 h).

concentration, the value of G/R has a larger decrease (Fig. 13b), this is because that the ET processes between the same energy levels of adjacent Er^{3+} ions can subsequently suppress the population in excited levels of $^2H_{11/2}$ and $^4S_{3/2}$, resulting in the decrease of green emissions. And during this process, the $^4F_{9/2}$ level has more advantage, resulting in the increase of red emissions, with the increase of Er^{3+} doping concentration⁴⁷. At the same time, the CR1 and CR2 processes can also decrease the value of G/R . Therefore, with the increase of Er^{3+} doping concentration, the ET1, ET2 and CR1 processes compose the dynamic circulatory energy transfer process occurred between adjacent Er^{3+} ions and become ever more active, so that the fluorescent lifetime of $^4I_{13/2}$ and $^4I_{11/2}$ levels have a remarkable decrease. Due to this kind of energy cycle process, although the fluorescent lifetime of upper level ($^4I_{11/2}$) is shorter than that of lower level ($^4I_{13/2}$), the population inversion between the two

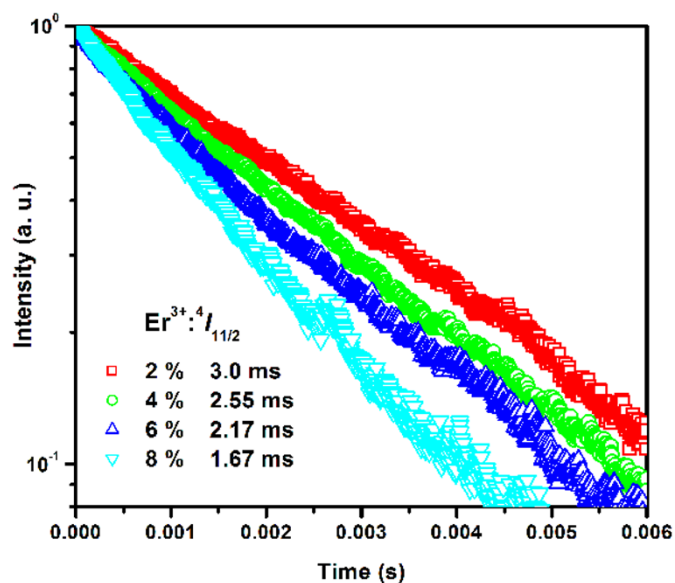


Figure 15 | The fluorescence decay curves of the $\text{Er}^{3+}:^4I_{11/2}$ level ($2.7 \mu\text{m}$ emission) in $x\text{Er}^{3+}$ ($x = 2, 4, 6, 8 \text{ mol}\%$) doped YOF submicron-crystals (calcined at 1100°C for 2 h).

levels is well achieved and the $2.7 \mu\text{m}$ emission can be obtained and enhanced, with the increase of Er^{3+} doping concentration.

In conclusion, Er^{3+} doped pure rhombohedral phase YOF submicron-crystals were synthesized by the crystalline phase transformed from pure orthorhombic YF_3 submicron-crystals, which were prepared by co-precipitation method and continuous calcining method. And the formation process of YOF submicron-crystals with quasi-spherical morphology mainly contains four steps, “growing”, “self-assemble”, “dissolution-recrystallization” and “growing” processes. Meanwhile, during the process of chemical synthesis, utilized the hygroscopic property of NH_4HF_2 to remove the OH^- in the structure of crystal particles, and the content of OH^- was obviously decrease, as confirmed by FTIR spectra. Moreover, with the Er^{3+} concentration increasing from 2 to 4 mol%, the $2.7 \mu\text{m}$ and 800 nm emissions

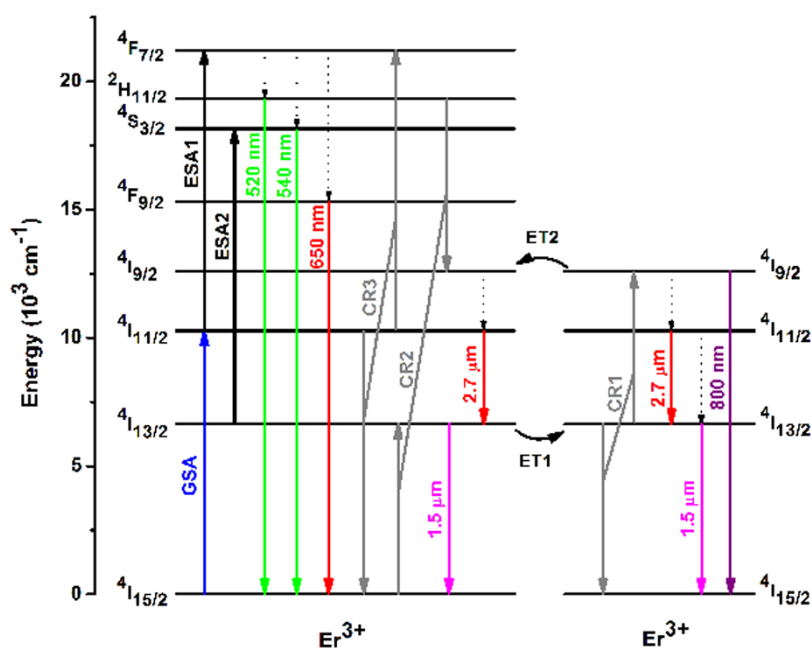


Figure 16 | The energy levels of Er^{3+} with relative transitions and the energy transfer processes between adjacent Er^{3+} ions.



were remarkably enhanced, as well as the decrease of 1.5 μm emission and value of G/R . And the fluorescent lifetime of the ${}^4I_{11/2}$ and ${}^4I_{13/2}$ levels obviously decreased with the increase of Er^{3+} doping concentration, due to the crucial dynamic circulatory energy transfer process ($\text{Er}^{3+}: {}^4I_{13/2} + {}^4I_{13/2} \rightarrow {}^4I_{15/2} + {}^4I_{9/2}$, $\text{Er}^{3+}: {}^4I_{13/2} \rightarrow \text{Er}^{3+}: {}^4I_{13/2}$, and $\text{Er}^{3+}: {}^4I_{11/2} \rightarrow \text{Er}^{3+}: {}^4I_{11/2}$) between adjacent Er^{3+} ions in YOF crystalline lattices become ever more active with the increase of Er^{3+} doping concentration. The population inversion is well achieved between the ${}^4I_{11/2}$ and ${}^4I_{13/2}$ levels through this dynamic circulatory energy transfer process.

In this paper, Er^{3+} doped YOF submicron-crystals with mid-infrared fluorescence were synthesized for the first time. Through the combination with glass matrixes to form nanocrystals/submicron-crystals-glass composites¹¹, it is expected to open a brand new field for the realization of mid-infrared micro/nano-lasers.

Methods

The aqueous solutions of Y^{3+} and Er^{3+} were mixed together to yield the desired stoichiometry of the final submicron-crystals ($\text{Y}_{1-x}\text{Er}_x\text{F}_3$, $x = 0, 0.02, 0.04, 0.06, 0.08$ (in mol)). This mixed aqueous solution was added dropwise into an aqueous solution of NH_4HF_2 (analytical grade) under magnetic stirring at room temperature and the dropping rate was kept at about 2 mL/min. During titration process, ammonium hydroxide ($\text{NH}_3 \cdot \text{H}_2\text{O}$, analytical grade) was used to adjust the pH value of the mixed solution and the final pH was in the range of 4–5⁴⁸. Then, the mixed solution was aging for 3 h at room temperature. The fluoride precursor nanopowders were centrifuged and washed with water and ethanol several times to remove residual ammonia and nitric ions. After dried at 80°C for 12 h, the fluoride precursor powders were crushed and calcined in air muffle furnace with a heating rate of 3°C/min and holden at different temperatures for 2 h. Finally, the corresponding submicron-crystals were obtained.

The crystalline structures of YF_3 and YOF submicron-crystals were observed using X-ray diffraction (XRD) on a D8 advance X-ray diffractometer (Bruker, Switzerland) with Cu K α radiation ($\lambda = 1.54056 \text{ \AA}$) and a scanning speed of 0.2°/min. The morphology and size distribution of the powders were observed by field emission-scanning electron microscopy (FE-SEM, Nova NanoSEM430, FEI, Netherlands) equipped with an energy-dispersive X-ray spectrometer (EDS) and high-resolution transmission electron microscopy (HR-TEM, 2100F, JEOL, Japan). Thermal analysis of the precursor powders were conducted using simultaneous thermal analyzer (STA, STA449C/3/MFC/GJUPITEY, NETZSCH, Germany). A heating rate of 10°C/min was adopted. The contents of OH^- in the crystal particles were estimated from Fourier transform-infrared spectroscopy (FTIR, Vector-33, Bruker, Switzerland). The photoluminescence spectra were measured on a Triax 320 spectrometer (Jobin-Yvon Co., France) with a resolution of 0.5 nm, which were excited by a 976 nm laser diode (LD) and detected with a PbSe photodetector. The fluorescence lifetime of $\text{Er}^{3+}: {}^4I_{11/2}$ and ${}^4I_{13/2}$ levels were measured on a Digital Phosphor Oscilloscope (TDS3012C, Tektronix, America) equipped on the Triax 320 spectrometer. All the measurements were carried out at room temperature.

- Sanamyan, T., Kanskar, M., Xiao, Y., Kedlaya, D. & Dubinskii, M. $\text{Er}^{3+}:\text{Y}_2\text{O}_3$ laser with nearly quantum defect-limited efficiency. *Opt. Express* **19**, 1082–1087 (2011).
- Dickinson, B. C., Golding, P. S., Pollnau, M., King, T. A. & Jackson, S. D. Investigation of a 791 nm pulsed-pumped 2.7 μm Er-doped ZBLAN fiber laser. *Opt. Commun.* **191**, 315–321 (2001).
- Zajac, A., Skorczakowski, M., Swiderski, J. & Nyga, P. Electrooptically Q-switch mid-infrared Er:YAG laser for medical applications. *Opt. Express* **12**, 5125–5130 (2004).
- Camargo, de A. S. S. *et al.* 2.8 and 1.55 μm emission from diode-pumped Er^{3+} -doped and Yb^{3+} co-doped lead lanthanum zirconate titanate transparent ferroelectric ceramic. *Appl. Phys. Lett.* **86**, 241112 (2005).
- Shaw, L. B., Cole, B., Thielen, P. A., Sanghera, J. S. & Aggarwal, I. D. Mid-wave IR and long-wave IR laser potential of rare-earth doped chalcogenide glass fiber. *J. Quantum Electron.* **37**, 1127–1137 (2001).
- Urquhart, P. Review of rare earth doped fiber lasers and amplifiers. *IEE Proc. J. Optoelect.* **135**, 385–407 (1988).
- Wang, F. *et al.* Tuning upconversion through energy migration in core-shell nanoparticles. *Nature Mater.* **10**, 968–973 (2011).
- Wang, F. *et al.* Simultaneous phase and size control of upconversion nanocrystals through lanthanide doping. *Nature* **463**, 1061–1065 (2010).
- Wang, X., Zhuang, J., Peng, Q. & Li, Y. D. A general strategy for nanocrystal synthesis. *Nature* **437**, 121–124 (2005).
- Jia, R., Yang, W., Bai, Y. & Li, T. Upconversion photoluminescence of $\text{ZrO}_2:\text{Er}^{3+}$ nanocrystals synthesized by using butadiol as high boiling point solvent. *Opt. Mater.* **28**, 246–249 (2006).
- Chai, G. Q., Dong, G. P., Qiu, J. R., Zhang, Q. Y. & Yang, Z. M. 2.7 μm Emission from transparent Er^{3+} , Tm^{3+} codoped Yttrium Aluminum Garnet ($\text{Y}_3\text{Al}_5\text{O}_{12}$) nanocrystals-tellurate glass composites by novel comelting technology. *J. Phys. Chem. C* **116**, 19941–19950 (2012).

- Fan, J. T. *et al.* Intense photoluminescence at 2.7 μm in transparent $\text{Er}^{3+}:\text{CaF}_2$ -fluorophosphate glass microcomposite. *Opt. Lett.* **36**, 4347–4349 (2011).
- Eichhorn, M. Quasi-three-level solid-state lasers in the near and mid infrared based on trivalent rare earth ions. *Appl. Phys. B* **93**, 269–316 (2008).
- Zhu, X. S. & Jain, R. *Mid-infrared coherent sources conference, Barcelona, Spain, paper Tu7* (2005).
- Jackson, S. D. Single-transverse-mode 2.5 W holmium-doped fluoride fiber laser operating at 2.86 μm . *Opt. Lett.* **29**, 334–336 (2004).
- Jackson, S. D. Continuous wave 2.9 μm dysprosium-doped fluoride fiber laser. *Appl. Phys. Lett.* **83**, 1316–1318 (2003).
- Wen, L., Wang, J. R., Hu, L. L. & Zhang, L. Y. Sensitizing effect of Nd^{3+} on the $\text{Er}^{3+}:$ 2.7 μm emission in fluorophosphate glass. *Chin. Opt. Lett.* **9**, 121601 (2011).
- Lin, H., Chen, D. Q., Yu, Y. L., Yang, A. P. & Wang, Y. S. Enhanced mid-infrared emissions of Er^{3+} at 2.7 μm via Nd^{3+} sensitization in chalcogenide glass. *Opt. Lett.* **36**, 1815–1817 (2011).
- Guo, Y. Y. *et al.* Enhanced 2.7 μm emission and energy transfer mechanism of $\text{Nd}^{3+}/\text{Er}^{3+}$ co-doped sodium tellurite glasses. *J. Appl. Phys.* **110**, 013512 (2011).
- Xu, R. R., Tian, Y., Hu, L. L. & Zhang, J. J. Enhanced emission of 2.7 μm pumped by laser diode from $\text{Er}^{3+}/\text{Pr}^{3+}$ -codoped germanate glasses. *Opt. Lett.* **36**, 1173–1175 (2011).
- Tikhomirov, V. K., Méndez-Ramos, J., Rodríguez, V. D., Furniss, D. & Seddon, A. B. Laser and gain parameters at 2.7 μm of Er^{3+} -doped oxyfluoride transparent glass-ceramics. *Opt. Mater.* **28**, 1143–1146 (2006).
- Pollnau, M. *et al.* Investigation of diode-pumped 2.8 μm laser performance in $\text{Er}:\text{BaY}_2\text{F}_8$. *Opt. Lett.* **21**, 48–50 (1996).
- Park, S. H., Lee, D. C., Heo, J. & Shin, D. W. Energy transfer between Er^{3+} and Pr^{3+} in chalcogenide glasses for dual-wavelength fiber-optic amplifiers. *J. Appl. Phys.* **91**, 9072–9077 (2002).
- Labbe, C., Doualan, J. L., Camy, P., Moncorgé, R. & Thuau, M. The 2.8 μm laser properties of Er^{3+} doped CaF_2 crystals. *Opt. Commun.* **209**, 193–199 (2002).
- Tu, D. T. *et al.* Time-resolved FRET biosensor based on amine-functionalized lanthanide-doped NaYF_4 nanocrystals. *Angew. Chem. Int. Ed.* **50**, 1–6 (2011).
- Liu, Y. S. *et al.* Amine-functionalized lanthanide-doped Zirconia nanoparticles: optical spectroscopy, time-resolved fluorescence resonance energy transfer biodetection, and targeted imaging. *J. Am. Chem. Soc.* **134**, 15083–15090 (2012).
- Capobianco, J. A., Boyer, J. C., Vetrone, F., Spgehini, A. & Bettinelli, M. Optical spectroscopy and upconversion studies of Ho^{3+} -doped bulk and nanocrystalline Y_2O_3 . *Chem. Mater.* **14**, 2915–2921 (2002).
- Pecoraro, E., Sousa, de D. F., Lebullenger, R., Hernandez, A. C. & Nunes, L. A. O. Evaluation of the energy transfer rate for the $\text{Yb}^{3+}:\text{Pr}^{3+}$ system in lead fluoroindogallate glasses. *J. Appl. Phys.* **86**, 3144–3148 (1999).
- Tick, P., Borrelli, N., Cornelius, L. & Newhouse, M. Transparent glass ceramics for 1300 nm amplifier applications. *J. Appl. Phys.* **78**, 6367–6374 (1995).
- Mortier, M., Goldner, P., Chateau, C. & Genotelle, M. Erbium doped glass-ceramics: concentration effect on crystal structure and energy transfer between active ions. *J. Alloys Comp.* **245**, 323–324 (2001).
- Li, G. G. *et al.* Electrospinning derived one-dimensional $\text{LaOCl}:\text{Ln}^{3+}$ ($\text{Ln} = \text{Eu}/\text{Sm}, \text{Tb}, \text{Tm}$) nanofibers, nanotubes and microbelts with multicolor-tunable emission properties. *Adv. Funct. Mater.* **20**, 3446–3456 (2010).
- Yan, R. X. & Li, Y. D. Down/Up conversion in Ln^{3+} -doped YF_3 nanocrystals. *Adv. Funct. Mater.* **15**, 763–770 (2005).
- Stouwdam, J. W. & Veggel, van F. C. J. M. Near-infrared emission of redispersible Er^{3+} , Nd^{3+} , and Ho^{3+} doped LaF_3 nanoparticles. *Nano Lett.* **2**, 733–737 (2002).
- Lemyre, J. L. & Ritcey, A. M. Synthesis of lanthanide fluoride nanoparticles of varying shape and size. *Chem. Mater.* **17**, 3040–3043 (2005).
- Tsujiuchi, K., Okada, A., Matsuura, D. & Soga, K. Development of flexible and transparent upconversion display by using polymer-ceramics composite. *J. Photopolym. Sci. Technol.* **22**, 541–546 (2009).
- Meijer, J. M., Aarts, L., Ende, van der B. M., Vluset, T. J. H. & Merijerink, A. Down conversion for solar cells in $\text{YF}_3:\text{Nd}^{3+}$, Yb^{3+} . *Phys. Rev. B* **81**, 035107 (2010).
- Li, G. G. *et al.* Tm^{3+} and/or Dy^{3+} doped LaOCl nanocrystalline phosphors for field emission displays. *J. Mater. Chem.* **19**, 8936–8943 (2009).
- Shang, M. M. *et al.* $\text{LaOF}:\text{Eu}^{3+}$ nanocrystals: hydrothermal synthesis, white and color-tuning emission properties. *Dalton Tran.* **41**, 5571–5580 (2012).
- Levin, I., Huang, Q. Z., Cook, L. P. & Wong-Ng, W. Nonquenchable chemical order-disorder phase transition in Yttrium Oxyfluoride. *Eur. J. Inorg. Chem.* 87–91 (2005).
- Fujihara, S., Koji, S., Kadota, Y. & Kimura, T. Phase-selective pyrolysis and Pr^{3+} luminescence in a $\text{YF}_3\text{-Y}_2\text{O}_3$ system from a single-source precursor. *J. Am. Ceram. Soc.* **87**, 1659–1662 (2004).
- Xu, Z. H. *et al.* Self-templated and self-assembled synthesis of nano/microstructures of Gd-based rare-earth compounds: morphology control, magnetic and luminescence properties. *Phys. Chem. Chem. Phys.* **12**, 11315–11324 (2010).
- Dong, G. P. *et al.* Morphology and phase control of fluorides nanocrystals activated by lanthanides with two-model luminescence properties. *Nanoscale* **4**, 4658–4666 (2012).
- Lichstein, B. M. & Woolf, C. *Process for the preparation of Ammonium Bifluoride from Ammonium Fluoride*. U. S. Patent 3,705,007, December 5 (1972).
- Lage, M. M., Righi, A., Matinaga, F. M., Gesland, J. Y. & Moreira, R. L. Raman-spectroscopic study of lanthanide trifluorides with the $\beta\text{-YF}_3$ structure. *J. Phys.: Condens. Matter* **16**, 3207–3218 (2004).



45. Wojciechowski, J., Pawelska, I., Grodecki, R. & Szymanski, L. Infrared to visible conversion in YOF:Yb³⁺, Ho³⁺ and YF₃:Yb³⁺, Ho³⁺ phosphors. *J. Electrochem. Soc.* **122**, 312–314 (1975).
46. Pollnau, M. & Jackson, S. D. Erbium 3 μm fiber lasers. *IEEE J. Sel. Top. Quantum Electron.* **7**, 30–40 (2001).
47. Dong, G. P. *et al.* Photoluminescence of Ag nanoparticle embedded Tb³⁺/Ce³⁺ codoped NaYF₄/PVP nanofibers prepared by electrospinning. *IEEE Photo. Techn. Lett.* **20**, 57–59 (2009).
48. Li, G. Y., Ni, Y. H., Hong, J. M. & Liao, K. M. Controllable synthesis of polyhedral YF₃ microcrystals via a potassium sodium tartrate-assisted hydrothermal route. *Cryst. Eng. Comm.* **10**, 1681–1686 (2008).

Acknowledgements

This research was supported by the China State 863 Hi-tech Program (2011AA030203), the NSFC (U0934001, 60977060, 51102096), the Guangdong Province and Hong Kong Invite Public Bidding Program (TC10BH07-1), the Science and Technology Project of Guangdong (2009A090100044, 2009B091300127, cgzhzd0903, 2010B2101230), the Project of Education Department of Guangdong Province (2009N9100200), the Fundamental Research Funds for the Central Universities (2009ZM0219, 2011ZG0005, 2011ZB0001), the

open research fund of state key laboratory of precision spectroscopy and the YNSF of SCUT (E5090880). The authors are grateful to Dr. Liaolin Zhang, Dr. Dechao Yu and Dr. Ying Tian for fruitful discussions.

Author contributions

G.P.D. proposed and guided the overall project. G.Q.C performed all experiments and analyzed the result. All the authors discussed the results. G.Q.C. and G.P.D. wrote the manuscript, with comments from J.R.Q., Q.Y.Z. and Z.M.Y.

Additional information

Competing financial interests: The authors declare no competing financial interests.

License: This work is licensed under a Creative Commons Attribution-NonCommercial-NoDerivs 3.0 Unported License. To view a copy of this license, visit <http://creativecommons.org/licenses/by-nc-nd/3.0/>

How to cite this article: Chai, G., Dong, G., Qiu, J., Zhang, Q. & Yang, Z. Phase Transformation and Intense 2.7 μm Emission from Er³⁺ Doped YF₃/YOF Submicron-crystals. *Sci. Rep.* **3**, 1598; DOI:10.1038/srep01598 (2013).